MECE E3028 Mechanical Engineering Laboratory II
Professor Qiao Lin
Spring 2022

Experiment E1: Low-Speed Wind Tunnel

LABORATORY REPORT

Lab Group 12

Axel Ortega

Anton Deti

Bruno Rergis

Arlene Diaz

Christine Zou

Ashton Buchanan

Samuel Adeniyi

Columbia University
Department of Mechanical Engineering

February 16, 2022

Contents

Acknowledgements **3**

Abstract **4**

List of Figures **5**

List of Tables **5**

1 Introduction **6**

2 Theory **6**
2.1 Airfoils, Spheres, and their Behavior in a Wind Tunnel 6
2.2 Lift and Drag Forces 7
2.2.1 Lift and Drag Coefficients 8
2.2.2 Angle of Attack and Stall Condition 8
2.2.3 Lift and Drag Coefficients vs. Angle of Attack 9
2.2.4 Lift from Pressure Distribution 9
2.2.5 Boundary Layers in Turbulent and Laminar Flows 10
2.3 Experimental Setup 11

3 Apparatus and Approach **11**
3.1 Apparatus 11
3.2 Approach 12

4 Results **13**

5 Discussion **14**
5.1 Lift Coefficient Calculations 14
5.2 Ball Drag Coefficients 15
5.3 Uncertainty Analysis 15
5.4 Lift Force Uncertainty using Pressure 15
5.5 C_D Uncertainty of Airfoil using Force 16
5.6 C_L Uncertainty of Airfoil Using Force 16
5.7 C_D Uncertainty Calculation of Smooth and Rough Sphere 16

6 Conclusion **17**

References **18**

A Appendix **19**
A.1 Wind Tunnel Calibration Chart 19
A.2 Channel Pressures at 25 Hz 19
A.3 Channel Pressures at 40 Hz 20

A.4 Ball Comparison 22
A.5 Airfoil at Different Angles of Attack 23

Acknowledgements

Thanks to Professor Qiao Lin, as well as TAs Kechun Wen and Wenting Dai for their guidance and support throughout the experiment.

Abstract

Low speed wind tunnel testing has evolved over the last century and has become a fundamental in the development of aviation vehicles. In aerodynamics, the design of airfoils is essential for determining an airplane's performance, stability, and control characteristics. Thus, this experiment studies a symmetrical, NACA0012 airfoil in a low speed wind turbine to learn about its kinematic and dynamic properties. A manometer is incorporated to measure the air pressure throughout the experiment, while a dynamometer is used to measure the lift and drag forces acting on the airfoil. The drag force is further studied through two different spheres - a smooth and a rough sphere - at various wind speeds. A LabView system is used with measurement computing DAQ (data acquisition) for direct access to lift and drag forces data obtained. The lift coefficients found for the airfoil are not similar to those published by NASA for the angle of attack of 9 degrees, however, due to its very low Reynold's number, there is little literature to determine its true value.

List of Figures

1 NACA0012 airfoil . . . 7
2 Airfoil Nomenclature . . . 7
3 Lift and Drag on an Airfoil with Respective Angle of Attack . . . 8
4 Drag Coefficient vs. Angle of Attack for Experimental NACA0012 airfoil . . . 9
5 Lift Coefficient vs. Angle of Attack for Experimental NACA0012 Airfoil . . . 9
6 Pressure Distribution of Symmetric Airfoil at 0 and 9 degrees of attack . . . 10
7 Comparison of laminar and turbulent flow profiles at boundary layers. . . . 10
8 Airfoil in wind tunnel testing section. . . . 12
9 Vishay system used to measure drag and lift. . . . 12
10 Dynamometer used to measure drag and lift. . . . 12
11 NACA Airfoil 0012 C_D vs. α at 25 Hz . . . 13
12 NACA Airfoil 0012 C_L vs. α at 25 Hz . . . 13
13 NACA Airfoil 0012 C_L/C_D vs. α at 25 Hz . . . 13
14 NACA Airfoil 0012 C_D vs. α at 40 Hz . . . 14
15 NACA Airfoil 0012 C_L vs. α at 40 Hz . . . 14
16 NACA Airfoil 0012 C_L/C_D vs. α at 40 Hz . . . 14
17 Semi-Log Plot of Drag Coefficient vs. Reynold's Number for Smooth and Rough Spheres . . . 14
18 Log Plot of Drag Coefficient vs. Reynold's Number for Smooth and Rough Spheres . . . 14
19 Wind Tunnel Calibration Chart . . . 19

List of Tables

1 Channel Pressures at 25 Hz and $\alpha = 9°$ . . . 19
2 Channel Pressures at 25 Hz and $\alpha = 0°$ . . . 20
3 Channel Pressures at 25 Hz and $\alpha = -9°$ . . . 20
4 Channel Pressures at 40 Hz and $\alpha = 9°$ . . . 20
5 Channel Pressures at 40 Hz and $\alpha = 0°$ . . . 21
6 Channel Pressures at 40 Hz and $\alpha = -9°$ . . . 21
7 Smooth Ball Raw Data . . . 22
8 Rough Ball Raw Data . . . 22
9 Data from Airfoil at Different Angles of Attack at 25 Hz . . . 23
10 Data from Airfoil at Different Angles of Attack at 40 Hz . . . 23

1 Introduction

Researchers use wind tunnels to learn more about how aircraft's fly. Wind tunnels are large tubes with large fans that move air at desired speeds to emulate flight conditions; test objects are fastened in the tunnel so they do not move. Smoke or dye can be used in the tunnel to help visualize the air movement as well as tying strings to the object itself.

Studying wind tunnels is important because companies and government agencies such as NASA, are always trying to improve air transportation and safety. With the research from wind tunnels, new designs and materials for airplanes can be found. Modeling in the wind tunnel is done by changing wind velocity and the angle of attack. The angle of attack is an important shape parameter because the lift and drag increase as the angle of attack increases up to a point. Once this point is reached - the stall angle - the airflow across the upper surface of the airfoil is detached causing the lift to steeply drop (1).

Airfoils such as the one shown in Figure 1 are NACA - National Advisory Committee for Aeronautics - airfoils. There are generally two types of airfoils: laminar flow and conventional. Laminar flow airfoils were originally developed to make an airplane fly faster. The laminar flow wing is usually thinner than the conventional airfoil; the leading edge is also more pointed and its upper and lower surfaces are nearly symmetrical. However, the most important difference between the airfoils is that the thickest part of a laminar flow wing occurs at 50% chord, while in the conventional design, the thickest part is at 25% chord - the distance from the leading to the trailing edges of a wing (2).

The objective of this experiment is to measure the pressure, lift, and drag forces and coefficients of a NACA0012 airfoil as well as the drag forces and coefficients of two different spheres in a low speed wind tunnel. The NACA0012 airfoil has symmetrical properties, having an identical upper and lower surface and hence having zero camber. For this geometry, the airfoil will have zero lift and a relatively low drag force when positioned horizontally in the flow - at zero angle of attack. To gain better insight about the airfoil, its will be measured at various angles of attack to see how pressure, lift, and drag varies with the change in angle of attack. These measurements will be conducted at two wind speeds which equate to 25 Hz and 40 Hz. Additionally, the aerodynamic performance of spheres with a smooth and rough surface will be measured. This will be done at various wind speeds which correspond to fan frequencies ranging from 5 Hz to 60 Hz in 5 Hz increments.

2 Theory

2.1 Airfoils, Spheres, and their Behavior in a Wind Tunnel

An airfoil is a cross-sectional shape of an object whose motion through a gas is capable of generating lift. A wind tunnel will be used to measure the kinematic and dynamic properties on a symmetrical airfoil from a NACA0012 airplane.

Figure 1: NACA0012 airfoil

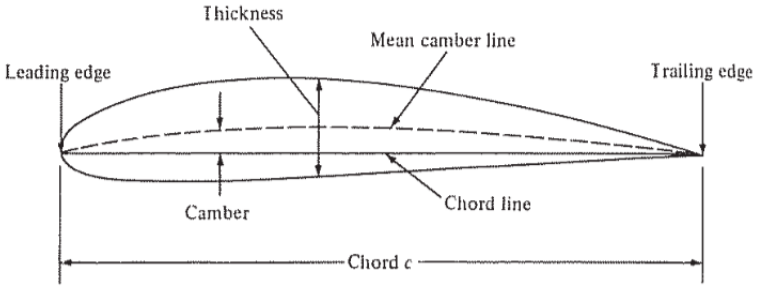

Figure 2: Airfoil Nomenclature

Figure 2 above displays the features in a NACA airfoil including mean camber line, leading edge, trailing edge, chord line, chord, and camber. NACA airfoils are airfoil shapes for aircraft wings developed by the National Advisory Committee for Aeronautics (NACA) (3). The shape of the NACA airfoils is described using a logical numbering system consisting of a series of digits following the word "NACA" (4). The first digit is a the maximum camber, the second digit is the location of maximum camber along the chord from the leading edge, and the last two digits give the maximum thickness(4). Camber is simply a measure of curvature in the airfoil. For this lab, a NACA0012 airfoil will be used, which means a symmetric airfoil with a maximum thickness of 12 percent(4). In a wind tunnel under test conditions, the NACA0012 airfoil experiences an aerodynamic force that is resolved into perpendicular and parallel components known as lift and drag, respectively (4).

2.2 Lift and Drag Forces

The lift force is an upward force that sustains an airplane in flight and is generated by flow around the wings. It arises from lower pressure on the upper surface of the wing and higher pressure on the lower surface(4).

$$L = Pwl \tag{1}$$

The drag force is a rearward force which acts opposite to the direction of the airplane's forward motion(4). The total drag can be further broken down into simply the addition of friction drag and form drag. These are drags due to viscous effects including skin friction and pressure imbalance(4).

2.2.1 Lift and Drag Coefficients

The lift coefficient, C_L, is a dimensionless quantity that relates the lift force on a solid body with solid body shape, Reynold's number Re, and Mach number, Ma (4).

Reynold's number is defined as:

$$Re = \frac{\rho U_\infty l}{\mu} \tag{2}$$

where ρ denotes the fluid density, U_∞ is free stream velocity, l is the characteristic body length, and μ is the fluid dynamic viscosity.

The Mach number, Ma, is defined using the speed of sound in the medium, c:

$$Ma = \frac{U_\infty}{c} \tag{3}$$

By combining Eq. 2 and Eq. 3, the equation for the lift coefficient can be derived. It is expressed as:

$$C_L = \frac{L}{\frac{1}{2}\rho U_\infty^2 A} \tag{4}$$

where L is the lift force, U_∞ is the same and A is the area of the solid body.

Similar to the lift coefficient in Eq. 4, the drag coefficient is a dimensionless quantity that relates the drag force to the solid body shape, Mach number, and Reynold's number. It is defined as

$$C_D = \frac{D}{\frac{1}{2}\rho U^2 A} \tag{5}$$

where D is drag force.

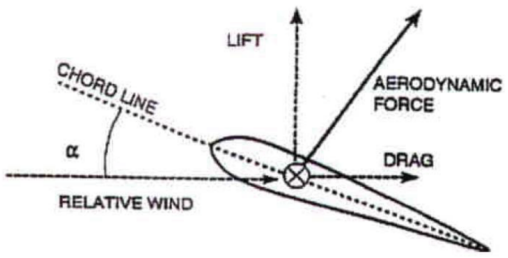

Figure 3: Lift and Drag on an Airfoil with Respective Angle of Attack

2.2.2 Angle of Attack and Stall Condition

The lift and drag coefficients measured at a particular air speed depend on the angle of attack α, which is the angle between free stream, or relative wind, U_∞ and chord line. When the angle of attack becomes too large, the lift force begins to drop. This defines the stall condition, or stall angle, which is dangerous for aviation and aircraft. The stalling angle of

attack is typically around 15° - 20° (5). The wing stalls as the angle of attack is increased beyond this value, and the lift coefficient drops rapidly while the drag coefficient continues to increase.

2.2.3 Lift and Drag Coefficients vs. Angle of Attack

As seen in Fig. 4, at a higher angle of attack, flow separation over the top surface of the airfoils is shown. Form drag due to flow separation begins to increase (4). Thus, as the angle of attack increases, the lift coefficient increases, which changes the amount of the induced drag. When the angle is zero, there is no lift, but drag can still be encountered.

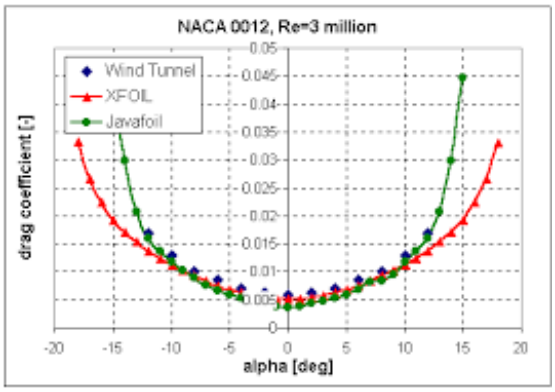

Figure 4: Drag Coefficient vs. Angle of Attack for Experimental NACA0012 airfoil

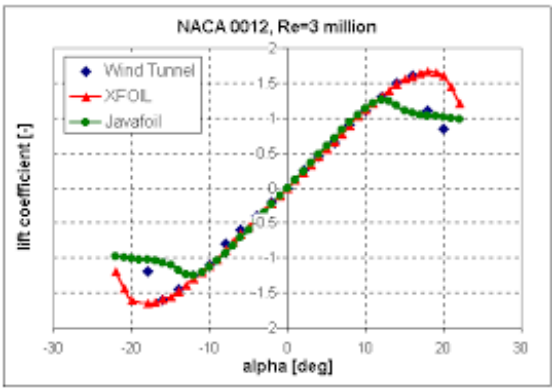

Figure 5: Lift Coefficient vs. Angle of Attack for Experimental NACA0012 Airfoil

The lift coefficient increases linearly from 0 when α is small. It will continue to increase linearly with the angle until it reaches a point where α becomes too large which is when the lift coefficient, C_L drops sharply. This relationship is shown in Fig. 5. At this point, drag increases significantly.

Note that the density of air varies with the ambient pressure, p_{amb} and temperature, T_i, which can influence the manner in which lift and drag coefficients are measured. The exact manner to calculate density of air is:

$$\rho_i = \frac{p_{amb}}{RT_i} \tag{6}$$

2.2.4 Lift from Pressure Distribution

To calculate lift, the area under the pressure distribution curve for a particular airfoil can be found.

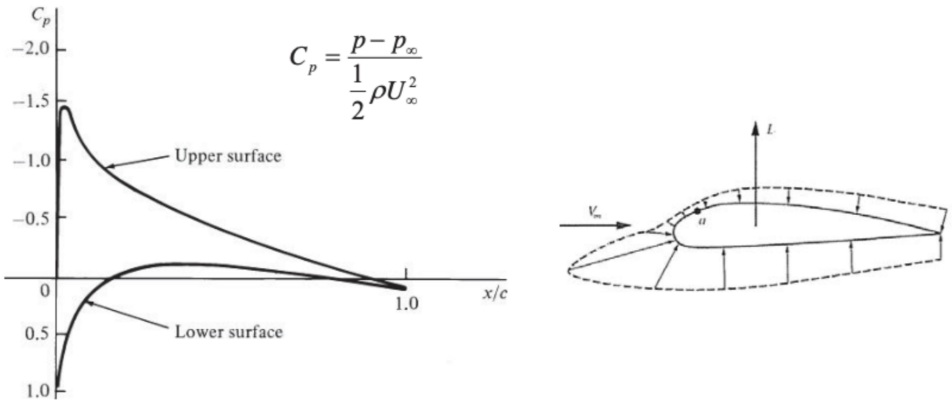

Figure 6: Pressure Distribution of Symmetric Airfoil at 0 and 9 degrees of attack

Figure 6 shows a rough schematic of the pressure distribution for a symmetric airfoil for various angles of attack. Such distributions mimic the distribution for this experiment. The net lift force can be found by integrating (or summing) the pressure times the area around the entire surface (6).

2.2.5 Boundary Layers in Turbulent and Laminar Flows

A boundary layer is a thin layer of a flowing gas or liquid in contact with a surface such as that of an airplane wing or of the inside of a pipe (7). In a laminar flow, streamlines are smooth and regular, and a fluid element moves smoothly along a streamline (8). This flow exhibits uniform flow properties at the boundary layer, as can be seen by the laminar profile in Figure 7. In turbulent flows, streamlines break up and fluid elements move in a random, irregular and tortuous fashion (8). This flow exhibits a "fuller" velocity profile because of stronger energy exchange between fluid particles (8). This can also be seen in Fig. 7.

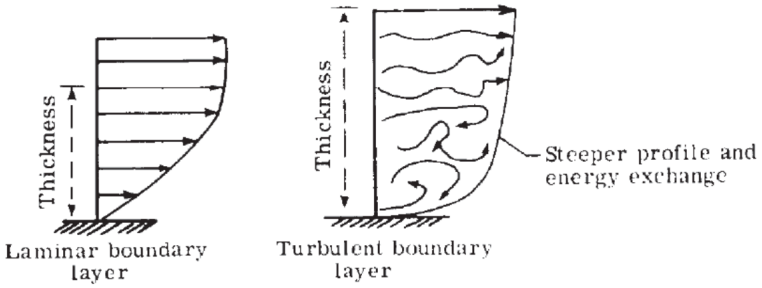

Figure 7: Comparison of laminar and turbulent flow profiles at boundary layers.

Laminar boundary layers flow more smoothly than turbulent boundary layers, and they produce significantly less friction drag than turbulent boundary layers.

Additionally, as the surface of the sphere becomes more rough, the boundary layer is disturbed and causes the transition to turbulence to occur at a lower Reynold's number as

well. This ultimately means that the drag crisis can be forced to occur at a significantly lower number.

The density of the air ρ_i is important for the wind tunnel because it affects the velocity and is important for comparing to next measurements. However, the air density cannot be measure directly, but can be calculated using Eq. 6. The air density is dependent on ambient temperature, p_{amb}, and temperature T_i, which is why it's necessary to obtain these measurements.

2.3 Experimental Setup

This experiment utilizes an airfoil, two spheres of varying roughness, a wind tunnel, a NACA0012 airfoil, a Vishay system, and several other instruments. In the first part of the lab, the wind tunnel is used to apply pressures at varying velocities on the airfoil. A manometer is used to measure the air pressures at nine different holes along the airfoil. In the second part of the lab, the test section in the wind tunnel is setup with a dynamometer, Vishay system, and a Lab VI program to determine the drag and lift felt by the spheres and airfoil. The wind tunnel is used in conjunction with the aforementioned tools to measure the air pressure, as well as the lift and drag forces on a symmetrical airfoil - the NACA0012 airfoil - shown in Fig. 1, and the drag force on two different spheres.

3 Apparatus and Approach

The symmetrical airfoil (NACA0012) with a chord length of 100 mm and a span length of 300 mm will be used. Two different spheres with a diameter of 42.67 mm will also be used. The wind tunnel is used in conjunction with the aforementioned tools to measure the air pressure, as well as the lift and drag forces on a symmetrical airfoil - the NACA0012 airfoil - shown in Fig. 1, and the drag force on two different spheres.

3.1 Apparatus

To measure the the pressure as well as the lift and drag forces on a symmetrical airfoil (NACA0012) and two different spheres with varying diameters, a wind tunnel, Vishay Strain Gauge Conditioner, Meriam Instrument red gauge oil manometer, a dynamometer, and various other hardwares will be used. Some of these instruments can be seen in Fig. 8 to Fig. 10.

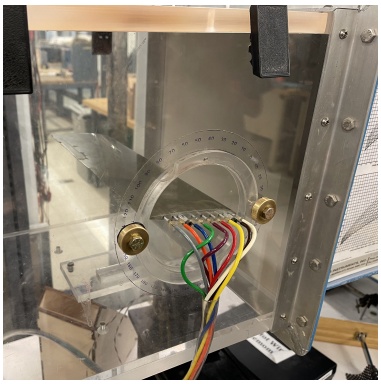

Figure 8: Airfoil in wind tunnel testing section.

Figure 9: Vishay system used to measure drag and lift.

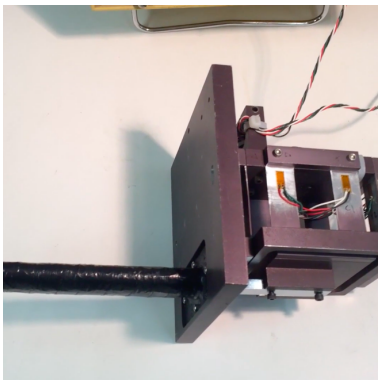

Figure 10: Dynamometer used to measure drag and lift.

3.2 Approach

Prior to the pressure measurement procedure, ensure that the top of the column of gauge oil in the manometer is zeroed perfectly. Make sure to measure the ambient pressure using a barometer.

To begin the pressure measurement procedure on the NACA0012 airfoil against the top side, insert the airfoil with nine small holes on its top surface into the wind tunnel's test section and mount it at an angle of attack of 9 degrees. Then, initiate the airflow fan at a frequency of 25 Hz using the operator interface panel on the wind tunnel. At this point, the pressures at all nine sensors can be recorded using the manometer. To switch between different holes on the airfoil, the mechanical box may be used to select between the different sensors.

Record measurements for nine pressures on the lower side of the airfoil at -9 degrees and 0 degrees as well. Then, repeat these steps for an airflow generated at a frequency of 40 Hz.

To begin the lift and drag measurement procedure on the two spheres, the dynamometer is mounted and secured tightly upside down in the test section such that the calibration steel rod faces upwards in the wind tunnel. Calibrate this instrument for lift by enabling the excitation voltage on channel 3 on the Vishay system. Make sure that the Vishay system is balanced by ensuring that the lights on channel 1 and 2 are extinguished.

Next, place the test weight on the steel rod and initiate and run the LabView VI Type the value for *Mean Lift Raw Voltage* into *Voltage Associated with Zero Lift*. While ensuring that the Vishay is still balanced, measure the mass of the calibration mass and plastic bracket and place it on top of the rod and balance channel 3. Run the program again and enter the value from *Mean Lift Raw Voltage* into *Voltage Associated with Lift Weight* and the value for mass in *Weight*.

To calibrate drag force, remove the calibration mass and bracket from the rod and insert a screw in its place. Turn on channel 2 while ensuring that the Vishay is balanced. Run the VI program again and enter the value from *Mean* into *Voltage Associated with Zero Drag*. Then, remove the top cover of the test setup assembly and place the stand with the pulley.

While ensuring that the Vishay is still balanced, carefully hang the calibration mass over the pulley. Next, run the VI program and enter the value for *Mean Drag Raw Voltage* into *Voltage Associated with Drag Weight*. As the mass suspends from the pulley, make sure that the drag force is the same as the calibration mass.

Once calibration is complete, disassemble the setup and mount the smooth sphere with the steel rod. Record measurements for drag for values ranging from 5 to 60 Hz in increments of 5 Hz. At each of these frequencies, calculate the corresponding Reynold's number and drag coefficient. Complete these steps for the rough sphere as well. Then, take measurements for the force on the airfoil by removing the steel rod from the dynamometer and then placing the wooden airfoil in that place instead. Begin adjusting the angle of attack by loosening the screws accordingly. Then, start the airflow and measure the lift and drag forces for 25 Hz at varying angles of attack. Repeat this procedure for an airfoil at 40 Hz.

4 Results

The raw data from the experiment is tabulated in Table 1 through Table 10 in Appendix A in Subsection A.2 through Subsection A.5.

The raw data in Table 1, Table 2, and Table 3 revealed a lift coefficient of 0.2036 for the NACA0012 airfoil at a fan frequency of 25 Hz and a lift coefficient of 0.2141 at a fan frequency of 25 Hz.

The data presented in Table 9 and Table 10 in the Appendix include the lift and drag coefficients of the NACA0012 airfoil at different angles of attack at fan frequencies of 25 Hz and 40 Hz respectively. Unsurprisingly both the drag and lift coefficients were higher when the fan frequency was at 40 Hz. The ratio between the lift and drag coefficients are also presented in these tables. C_L, C_D, and C_L/C_D, versus α for the airfoil are all plotted below in Figures 11-16.

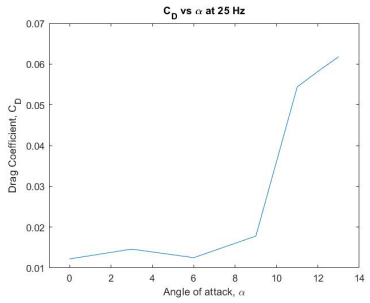

Figure 11: NACA Airfoil 0012 C_D vs. α at 25 Hz

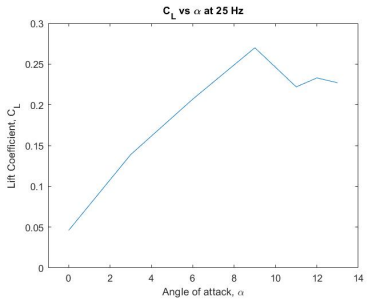

Figure 12: NACA Airfoil 0012 C_L vs. α at 25 Hz

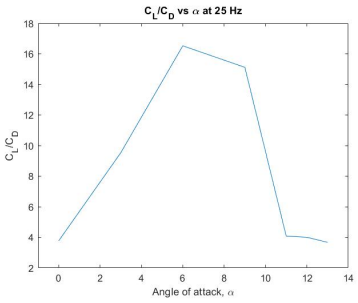

Figure 13: NACA Airfoil 0012 C_L/C_D vs. α at 25 Hz

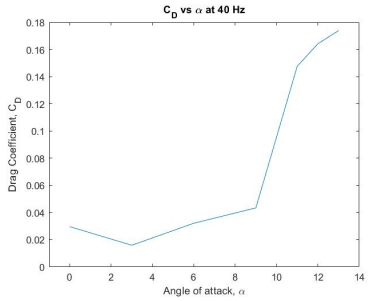

Figure 14: NACA Airfoil 0012 C_D vs. α at 40 Hz

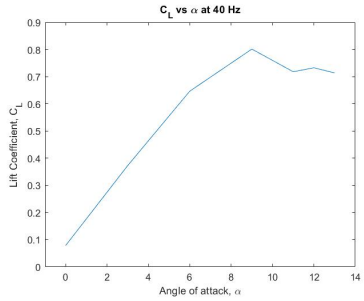

Figure 15: NACA Airfoil 0012 C_L vs. α at 40 Hz

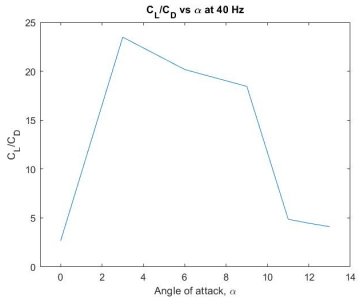

Figure 16: NACA Airfoil 0012 C_L/C_D vs. α at 40 Hz

Drag coefficients of each ball are tabulated in Table 7 and 8. The data revealed that the drag coefficient of the rough ball was usually lower than that of the smooth ball. These results were plotted in Fig. 17 and Fig. 18.

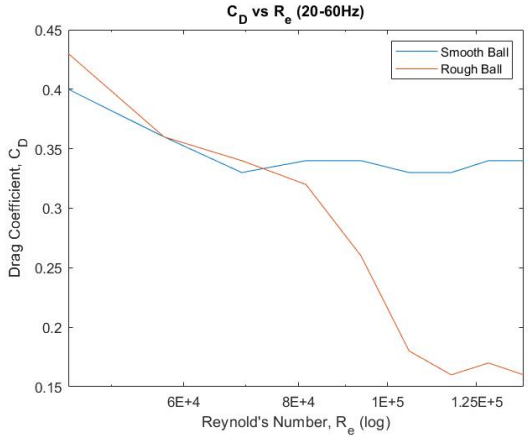

Figure 17: Semi-Log Plot of Drag Coefficient vs. Reynold's Number for Smooth and Rough Spheres

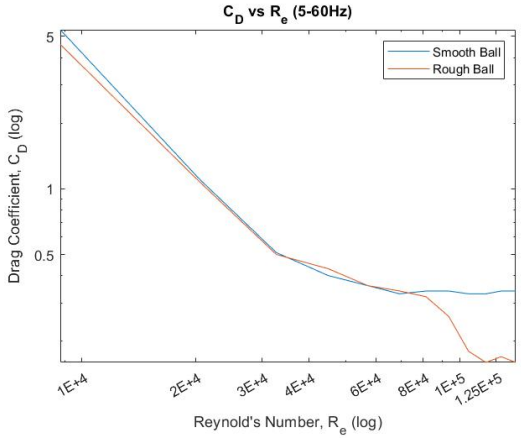

Figure 18: Log Plot of Drag Coefficient vs. Reynold's Number for Smooth and Rough Spheres

5 Discussion

5.1 Lift Coefficient Calculations

The lift coefficients found at angles of attack of 9° and −9° were found by calculating differential surface areas of the airfoil using linear approximations. These were then multiplied with the pressures recorded by the 9 pressure channels. This yielded differential forces across the entire airfoil which were then summed to find the total lift and drag forces acting on the wing; the difference of these two further yielded net lift which was used to calculate the lift coefficients using Eq. 4. Lift coefficients were not determined for angle of attack of 0° because the lift and drag would be equal on the airfoil at this angle regardless of the wind speed because of the airfoil symmetry; the pressures caused by the wind on the airfoil

surface would be equal on the top and bottom half of the airfoil meaning no lift or drag can be generated.

The lift coefficients found for the NACA0012 are not similar to those published by NASA for the angle of attack of 9°. However, for the very low Reynold's number in the given test conditions, there is very little literature to compare to; the NASA literature published values for a flow with a Reynold's number of 6 million which is not close to the test conditions of the experiment (9).

Additionally, according to this data, stall began to occur at an angle of attack of 11 degrees. The literature, from NASA, states that the stall angle should be 16 degrees. The angle difference is most likely due to the precision of the angle and pressure readings and/or wind turbine imperfections.

5.2 Ball Drag Coefficients

The drag coefficients of the balls, as previously mentioned are compared in Fig. 17 and Fig. 18. These figures demonstrate that for more laminar flows they act essentially identically in terms of their drag coefficients but the rough ball's drag coefficient decreases sharply in flows with Reynold's numbers of approximately 8×10^4. This is likely because the rough surface can counteract some of the drag forces caused by non-linear, irregular flows such as those in flows with higher Reynold's numbers.

5.3 Uncertainty Analysis

The uncertainties relevant in this experimentation follow from the general equation below. Where when considering the uncertainty of a calculated value r, its uncertainty is given through the equation below in which we consider x, y , and z variable in the equation for r each with their own specified uncertainty.

$$U_r \approx \sqrt{U_x^2(\frac{\partial r}{\partial x})^2 + U_y^2(\frac{\partial r}{\partial y})^2 + U_z^2(\frac{\partial r}{\partial z})^2 + ...} \tag{7}$$

More formally the absolute uncertainty of each variable (i.e. U_x, U_y, or U_z is measured through a combination of its bias and precision uncertainties.

$$U_x = \sqrt{{P_x}^2 + {B_x}^2}. \tag{8}$$

Applying Eq. (8) to each variable and then using those absolute uncertainties and applying them into Eq. (7), we can formally decide what the uncertainty of each calculated value is.

5.4 Lift Force Uncertainty using Pressure

Apply Eq.(1) to Eq. (7) to obtain:

$$U_L \approx \sqrt{U_P^2(wl)^2 + U_w^2(Pl)^2 + U_l^2(Pw)^2} \tag{9}$$

Where l is the length of the section where pressure is being applied, w is the width of the airfoil and P is the pressure of the fluid, air on that section. Applying this equation to each section where force is measured and then just as the total lift force is summed over all sections, the uncertainties summation would provide the uncertainty of the total lift force. Note that here we can take w to be a constant and thus $U_w = 0$. And as according to outline of the investigation
$U_P = 0.10$ x the pressure the uncertainty is being taken at.
$U_l = 0.10$ x the length of the section for which lift force is being found.

5.5 C_D Uncertainty of Airfoil using Force

Applying Eq. (5) to Eq. (7) and noting that the area A is simply the chord length multiplied by the airfoil's width we find.

$$U_{C_D} \approx \sqrt{U_D^2(\frac{2}{\rho V^2 lw})^2 + U_\rho^2(\frac{-2D}{\rho^2 V^2 lw})^2 + U_V^2(\frac{-4D}{\rho lw V^3})^2 + U_w^2(\frac{-2D}{\rho V^2 lw^2})^2 + U_l^2(\frac{-2D}{\rho V^2 l^2 w})^2} \tag{10}$$

5.6 C_L Uncertainty of Airfoil Using Force

Applying Eq. (4) into the Eq. (7)

$$U_{C_L} \approx \sqrt{U_L^2(\frac{2}{\rho V^2 lw})^2 + U_\rho^2(\frac{-2L}{\rho^2 V^2 lw})^2 + U_V^2(\frac{-4L}{\rho lw V^3})^2 + U_w^2(\frac{-2L}{\rho V^2 lw^2})^2 + U_l^2(\frac{-2L}{\rho V^2 l^2 w})^2} \tag{11}$$

5.7 C_D Uncertainty Calculation of Smooth and Rough Sphere

Applying Eq. (5) into the Eq. (7) but in this case using simply A for the cross sectional area as opposed to the variables l and w necessary for the airfoil.

$$U_{C_D} \approx \sqrt{U_D^2(\frac{2}{\rho V^2 A})^2 + U_\rho^2(\frac{-2D}{\rho^2 V^2 A})^2 + U_V^2(\frac{-4D}{\rho A V^3})^2 + U_A^2(\frac{-2D}{\rho V^2 A^2})^2} \tag{12}$$

Noting that we can take the density of the air and airfoil width as constant and from the outline of the lab we find that $U_w = 0$ and $U_\rho = 0$.
$U_V = 0.15$ x the wind speed the coefficient is being calculated at.
$U_A = 0.10$ x the area the coefficient is being measured at.

$U_D = 0.25$ x the force used to find the coefficient.
$U_l = 0.10$ x the length of the measured chord length
This applies to all of the above drag and lift coefficient uncertainty equations.

6 Conclusion

This experiment investigated the lift and drag forces on a symmetrical NACA0012 airfoil and the drag force on two different textured spheres, in a low-speed wind tunnel. With the use of the measurements for pressure, angle of attack, and wind velocity, the drag and lift properties were able to be found. The experiment allowed this group of engineer students to gain hands-on experience with the wind tunnel equipment as well as the dynamometers and manometers.

The main conclusions of the experiment were that the stall angle was determined to be 11°. Additionally, it was shown that rough surfaces have lower drag coefficient's in flows that are less laminar - i.e. in flows with higher Reynold's numbers. This is somewhat logical given the fact that the rough surface can allow for easier movement of unpredictable fluid flows.

References

[1] S. Brary, "Angle of attack," 2021.

[2] NASA, "Principle of flight," 2010.

[3] B. Allen, "Naca airfoils," 2017.

[4] K. Wen and Q. Lin, "Forces on immersed bodies and low-speed wind tunnel experiment," 2022.

[5] "Angle of attack."

[6] N. Hall, "Lift from pressure-area," 2021.

[7] T. E. of Encyclopaedia Britannica, "boundary layer."

[8] Q. Lin, "External flow review: Incompressible fluid flow around a solid body," 2022.

[9] C. Rumsey, "2dn00: 2d naca 0012 airfoil validation case," 2021.

Contributions by section:

- Abstract: Sam, Axel
- Introduction: Ashton, Sam
- Theory: Arlene, Axel
- Apparatus and Approach: Arlene, Christine, Axel
- Results: Bruno, Christine, Anton, Sam, Axel
- Discussion: Bruno, Anton
- Conclusions: Bruno, Ashton
- Appendix: Bruno, Christine

A Appendix

A.1 Wind Tunnel Calibration Chart

Frequency Sweep:		H2O/VDC:	1.982567				
Frequency(Hz)	VDC	ΔP("H2O)	u (m/s)*	u(fps)	RPM Motor	dBA(1)	dBA(2)
60	3.22	6.3839	51.451	168.800	1760	85	86
55	2.7	5.3529	47.114	154.570	1615	84	86
50	2.24	4.4410	42.913	140.789	1470	82	86
45	1.813	3.5944	38.607	126.661	1326	81	85.5
40	1.424	2.8232	34.215	112.253	1180	80	83
35	1.08	2.1412	29.797	97.759	1034	78	82
30	0.783	1.5523	25.371	83.238	888	76	81
25	0.53	1.0508	20.874	68.483	741	73	79

Figure 19: Wind Tunnel Calibration Chart

A.2 Channel Pressures at 25 Hz

Channel	Pressure (9 deg)	dA (m^2)	Force (N)
0	0	0	0
1	648.77454	0.001513560256	0.9819593587
2	634.99476	0.00168496224	1.069942193
3	468.51252	0.003243726384	1.519726422
4	449.38956	0.003161921894	1.420934689
5	429.14172	0.003124103086	1.340682972
6	437.2971	0.003105067028	1.357836807
7	389.77092	0.003086104693	1.202873865
8	370.92918	0.003070876514	1.139077707
9	351.525	0.003061547102	1.076210345

Table 1: Channel Pressures at 25 Hz and $\alpha = 9°$

Channel	Pressure (0 deg)	dA (m^2)	Force (N)
0	0	0	0
1	383.58408	0.001513560256	0.5805776183
2	395.39532	0.00168496224	0.6662261839
3	388.92726	0.003243726384	1.261573615
4	386.6775	0.003161921894	1.222644053
5	379.36578	0.003124103086	1.185177804
6	367.83576	0.003105067028	1.14215469
7	367.27332	0.003086104693	1.133443916
8	357.43062	0.003070876514	1.097625296
9	352.08744	0.003061547102	1.077932282

Table 2: Channel Pressures at 25 Hz and $\alpha = 0°$

Channel	Pressure (-9 deg)	dA (m^2)	Force (N)
0	0	0	0
1	205.85304	0.001513560256	0.3115709799
2	263.50314	0.00168496224	0.4439928409
3	300.9054	0.003243726384	0.9760547851
4	314.40396	0.003161921894	0.9941207646
5	322.84056	0.003124103086	1.00858719
6	327.34008	0.003105067028	1.016412889
7	334.37058	0.003086104693	1.031902616
8	334.6518	0.003070876514	1.027674353
9	331.8396	0.003061547102	1.015942566

Table 3: Channel Pressures at 25 Hz and $\alpha = -9°$

A.3 Channel Pressures at 40 Hz

Channel	Pressure (9 deg)	dA (m^2)	Force (N)
0	0	0	0
1	1727.53446	0.001513560256	2.614727499
2	1572.30102	0.00168496224	2.649267848
3	1249.46046	0.003243726384	4.05290786
4	1177.46814	0.003161921894	3.723062291
5	1110.53778	0.003124103086	3.469434506
6	1051.20036	0.003105067028	3.264047577
7	1002.5493	0.003086104693	3.093972099
8	952.77336	0.003070876514	2.925849335
9	905.80962	0.003061547102	2.773178817

Table 4: Channel Pressures at 40 Hz and $\alpha = 9°$

Channel	Pressure (0 deg)	dA (m^2)	Force (N)
0	0	0	0
1	993.83148	0.001513560256	1.504223829
2	1026.73422	0.00168496224	1.730008391
3	1021.67226	0.003243726384	3.314025266
4	1001.42442	0.003161921894	3.166425798
5	972.73998	0.003124103086	3.038939973
6	959.24142	0.003105067028	2.978508905
7	935.0565	0.003086104693	2.885682252
8	911.71524	0.003070876514	2.799764918
9	875.71908	0.003061547102	2.681055211

Table 5: Channel Pressures at 40 Hz and $\alpha = 0°$

Channel	Pressure (-9 deg)	dA (m^2)	Force (N)
0	0	0	0
1	458.10738	0.001513560256	0.6933731233
2	628.24548	0.00168496224	1.058569911
3	739.04616	0.003243726384	2.397263528
4	782.63526	0.003161921894	2.474631563
5	802.03944	0.003124103086	2.50565389
6	816.38166	0.003105067028	2.534919775
7	825.09948	0.003086104693	2.546343377
8	831.0051	0.003070876514	2.551914045
9	825.09948	0.003061547102	2.526080922

Table 6: Channel Pressures at 40 Hz and $\alpha = -9°$

A.4 Ball Comparison

Hz	Velocity of Wind	Mean Drag (KG)	Mean Drag (N)	Drag STD Dev	Drag Coefficient	Reynold's Number
5	3.206	0.004762	0.04671522	0.009124	5.36	8,767.84
10	7.477	0.005344	0.05242464	0.007562	1.11	20,448.26
15	11.96	0.006264	0.06144984	0.0067	0.51	32,708.46
20	16.421	0.009407	0.09228267	0.006897	0.40	44,908.50
25	20.874	0.01369	0.1342989	0.006361	0.36	57,086.66
30	25.371	0.01851	0.1815831	0.007656	0.33	69,385.15
35	29.797	0.02589	0.2539809	0.01398	0.34	81,489.47
40	34.215	0.03449	0.3383469	0.009446	0.34	93,571.91
45	38.607	0.04303	0.4221243	0.01108	0.33	105,583.25
50	42.913	0.05289	0.5188509	0.01147	0.33	117,359.39
55	47.114	0.06436	0.6313716	0.01431	0.34	128,848.37
60	51.451	0.07677	0.7531137	0.02342	0.34	140,709.29

Table 7: Smooth Ball Raw Data

Hz	Velocity of Wind	Drag Force (KG)	Drag Force (N)	Drag STD Dev	Drag Coefficient	Reynold's Number
5	3.206	0.004076	0.03998556	0.007773	4.59	8,767.84
10	7.477	0.005224	0.05124744	0.006839	1.08	20,448.26
15	11.96	0.006198	0.06080238	0.006053	0.50	32,708.46
20	16.421	0.01011	0.0991791	0.006704	0.43	44,908.50
25	20.874	0.01368	0.1342008	0.006473	0.36	57,086.66
30	25.371	0.01899	0.1862919	0.006965	0.34	69,385.15
35	29.797	0.02418	0.2372058	0.01237	0.32	81,489.47
40	34.215	0.02579	0.2529999	0.01236	0.26	93,571.91
45	38.607	0.02305	0.2261205	0.01165	0.18	105,583.25
50	42.913	0.02533	0.2484873	0.007343	0.16	117,359.39
55	47.114	0.03169	0.3108789	0.008139	0.17	128,848.37
60	51.451	0.03678	0.3608118	0.008232	0.16	140,709.29

Table 8: Rough Ball Raw Data

A.5 Airfoil at Different Angles of Attack

Angle of Attack	Drag Force (kg)	Mean Drag (N)	Drag STD Dev	Mean Lift (kg)	Mean Lift (N)	Lift STD Dev	Drag Coefficient	Lift Coefficient	$\frac{C_L}{C_D}$
0	0.02011	0.1972791	0.006433	0.07576	0.7432056	0.08419	0.01	0.05	3.7673
3	0.02406	0.2360286	0.006406	0.2292	2.248452	0.08695	0.01	0.14	9.5262
6	0.02058	0.2018898	0.006927	0.3401	3.336381	0.08065	0.01	0.21	16.5258
9	0.02932	0.2876292	0.008965	0.4433	4.348773	0.07921	0.02	0.27	15.1194
11	0.08942	0.8772102	0.01151	0.3647	3.577707	0.09705	0.05	0.22	4.0785
12	0.09562	0.9380322	0.02854	0.3824	3.751344	0.1039	0.06	0.23	3.9992
13	0.1016	0.996696	0.0268	0.3726	3.655206	0.1038	0.06	0.23	3.6673

Table 9: Data from Airfoil at Different Angles of Attack at 25 Hz

Angle of Attack	Drag Force (kg)	Mean Drag (N)	Drag STD Dev	Mean Lift (kg)	Mean Lift (N)	Lift STD Dev	Drag Coefficient	Lift Coefficient	$\frac{C_L}{C_D}$
0	0.0486	0.476766	0.008137	0.1294	1.269414	0.09242	0.03	0.08	2.6626
3	0.02609	0.2559429	0.007591	0.6126	6.009606	0.09345	0.02	0.37	23.4803
6	0.05269	0.5168889	0.007919	1.0627	10.425087	0.09367	0.03	0.65	20.1689
9	0.0714	0.700434	0.03139	1.317	12.91977	0.09086	0.04	0.80	18.4454
11	0.24257	2.3796117	0.03	1.18	11.5758	0.1587	0.15	0.72	4.8646
12	0.2699	2.647719	0.0313	1.2039	11.810259	0.1724	0.16	0.73	4.4605
13	0.2858	2.803698	0.03374	1.1729	11.506149	0.1995	0.17	0.71	4.1039

Table 10: Data from Airfoil at Different Angles of Attack at 40 Hz